

Frequency-dependent viscoelastic parameters of mouse brain tissue estimated by MR elastography

This article has been downloaded from IOPscience. Please scroll down to see the full text article.

2011 Phys. Med. Biol. 56 2391

(<http://iopscience.iop.org/0031-9155/56/8/005>)

View [the table of contents for this issue](#), or go to the [journal homepage](#) for more

Download details:

IP Address: 128.252.20.193

The article was downloaded on 23/03/2011 at 13:41

Please note that [terms and conditions apply](#).

Frequency-dependent viscoelastic parameters of mouse brain tissue estimated by MR elastography

E H Clayton^{1,4}, J R Garbow² and P V Bayly^{1,3}

¹ Department of Mechanical Engineering and Materials Science, Washington University in St Louis, 1 Brookings Drive, Campus Box 1185, Saint Louis, MO 63130, USA

² Biomedical Magnetic Resonance Laboratory, Department of Radiology, Washington University in St Louis, 4525 Scott Avenue, Campus Box 8227, Saint Louis, MO 63110, USA

³ Department of Biomedical Engineering, Washington University in St Louis, 1 Brookings Drive, Campus Box 1097, Saint Louis, MO 63130, USA

E-mail: clayton@wustl.edu, garbow@wustl.edu and pvb@wustl.edu

Received 7 December 2010, in final form 7 February 2011

Published 22 March 2011

Online at stacks.iop.org/PMB/56/2391

Abstract

Viscoelastic properties of mouse brain tissue were estimated non-invasively, *in vivo*, using magnetic resonance elastography (MRE) at 4.7 T to measure the dispersive properties of induced shear waves. Key features of this study include (i) the development and application of a novel MR-compatible actuation system which transmits vibratory motion into the brain through an incisor bar, and (ii) the investigation of the mechanical properties of brain tissue over a 1200 Hz bandwidth from 600–1800 Hz. Displacement fields due to propagating shear waves were measured during continuous, harmonic excitation of the skull. This protocol enabled characterization of the true steady-state patterns of shear wave propagation. Analysis of displacement fields obtained at different frequencies indicates that the viscoelastic properties of mouse brain tissue depend strongly on frequency. The average storage modulus (G') increased from approximately 1.6 to 8 kPa over this range; average loss modulus (G'') increased from approximately 1 to 3 kPa. Both moduli were well approximated by a power-law relationship over this frequency range. MRE may be a valuable addition to studies of disease in murine models, and to pre-clinical evaluations of therapies. Quantitative measurements of the viscoelastic parameters of brain tissue at high frequencies are also valuable for modeling and simulation of traumatic brain injury.

(Some figures in this article are in colour only in the electronic version)

⁴ Author to whom any correspondence should be addressed.

1. Introduction

1.1. Motivation: traumatic brain injury and other brain pathology

Traumatic brain injuries (TBI) are widespread in the United States and can result in permanent physical, cognitive, and/or behavioral impairment. Despite the prevalence and severity of TBI, the condition remains poorly understood and difficult to diagnose. Computer simulations of injury mechanics offer enormous potential for the study of TBI. Simulations can supplant experiments which are extremely difficult or expensive to perform, or cannot be performed for ethical reasons. However, computer models require accurate descriptions of tissue constitutive behavior and tissue connectivity (boundary conditions). Lacking such data, numerical predictions of brain deformation remain of questionable value. Quantifying tissue viscoelasticity is particularly important for understanding TBI, since rapid deformation of brain matter is a common feature among these injuries. MRE has also been suggested as a possible diagnostic or research tool for other brain disorders. Changes in material properties have been proposed as markers of tumor pathology (Muthupillai *et al* 1995) or progression of disease and degenerative processes, including Alzheimer's disease (Pattison *et al* 2010), multiple sclerosis (Wuerfel *et al* 2010), and aging (Sack *et al* 2009a).

1.2. Magnetic resonance elastography

Magnetic resonance elastography (MRE) is a non-invasive imaging technique for quantitative measurement of the mechanical properties of biological tissue (Muthupillai *et al* 1995). To perform MRE the standard nuclear magnetic resonance imaging (MRI) method is modified to measure displacements due to wave propagation. The basic data in MR images are the radio-frequency (RF) signals produced by the precession of nuclear spins; ^1H is the predominant nucleus of interest in biological imaging. An MRE pulse sequence contains additional, temporally varying, 'motion-sensitive' magnetic-field gradients which produce changes in spin-emitted RF signal phase that are proportional to spin displacement. These changes in spin phase can be measured throughout the imaging volume, producing displacement fields of high spatial resolution. Components of displacement in any direction can be measured by applying the motion-encoding gradients along that direction.

Several studies have explored the diagnostic value of MRE in the clinical setting. Interest has largely been driven by the empirical relationship between tissue health and stiffness. The mechanical properties of human tissues have been investigated using MRE. Plewes *et al* (2000) estimated isotropic elastic properties of breast tissue, whereas Sinkus *et al* (2005a, 2005b) probed both isotropic and anisotropic viscoelastic properties. MRE has been applied to the human brain (Kruse *et al* 2008, Hamhaber *et al* 2007), liver (Asbach *et al* 2008, Rouviere *et al* 2006, Yin *et al* 2007a), heart (Elgeti *et al* 2008, Sack *et al* 2009b, Robert *et al* 2009), and prostate (Kemper *et al* 2004).

Fewer MRE studies have been conducted in animals. MRE has been applied to the canine prostate (Chopra *et al* 2009), porcine heart (Kolipaka *et al* 2010), and the murine and bovine eye (Clayton *et al* 2010, Litwiller *et al* 2010). In most animal studies, the primary research objective has been to demonstrate proof-of-concept for implementation as a clinical diagnostic tool. MRE studies in animal models have considerable value for monitoring disease staging and effects of therapy (Diguët *et al* 2009, Murphy *et al* 2010, Pattison *et al* 2010, Schregel *et al* 2010, Yin *et al* 2007b). Of small animal models, the mouse is most frequently employed since it is low cost, small, relatively easy to handle, and its genomics are readily probed and manipulated.

Atay *et al* (2008) were the first to demonstrate feasibility of MR elastography in the mouse brain at 1200 Hz. Since then, others have performed studies at similar actuation frequencies (e.g., 1000, 1500 Hz) to investigate disease progression in the murine brain and its effect on mechanical tissue properties (Diguët *et al* 2009, Murphy *et al* 2010, Schregel *et al* 2010). The protocols of Atay *et al* (2008) and Murphy *et al* (2010) required an invasive procedure to affix the mechanical actuator to the mouse. Diguët *et al* (2009) and Schregel *et al* (2010) induced longitudinal waves into the skull using a mechanical transducer consisting of a coil and programmable pulse generator.

In this study, a novel, non-invasive, easy-to-use actuation setup was designed, built, and incorporated into animal studies. Mechanical vibrations were induced through an actuated incisor bar, allowing for efficient and well-tolerated studies. Experiments were performed at seven actuation frequencies, between 600 and 1800 Hz, to characterize the dispersive properties of mouse brain tissue. The analysis of experimental data was performed in three ways to cross-check results: (i) using a single component of the displacement field (the most efficient approach); (ii) using all three components of the three-dimensional (3D) displacement field, and (iii) using the curl of the 3D displacement field (to eliminate longitudinal wave contributions).

2. Methods

2.1. Acquisition of spatiotemporal wave fields

Later work by Muthupillai *et al* (1996) describes in detail the physics of measuring harmonically varying displacement fields with NMR spin-phase accumulation; the key points are summarized briefly in this section. Consider a single ^1H proton spin packet undergoing harmonic mechanical excitation and subjected to a sinusoidal, motion-encoding magnetic-field gradient, $G_i \sin(\omega_g \tau)$, parallel to an orthogonal reference coordinate i . The shift in NMR signal phase, θ_i , at position x_0, y_0, z_0 , is governed by

$$\theta_i(x_0, y_0, z_0, \Phi) = \gamma \int_0^t G_i \sin(\omega_g \tau) u_i \sin(\omega_d \tau + \Phi) d\tau \quad (\text{no sum on } i), \quad (1)$$

where G_i and ω_g are the motion-encoding gradient amplitude and oscillating frequency, respectively; $u_i(x_0, y_0, z_0)$ is the amplitude of the displacement component of the spin packet at this location and ω_d is the mechanical actuator driving frequency; γ is the gyromagnetic ratio of ^1H nuclei (protons). The synchronization delay, Φ , results in a temporal phase shift between the motion of a particular spin packet and the motion-encoding gradient. If multiple phase images are acquired, each with a different synchronization delay (corresponding to a fraction of the actuation period), a time history of spin phase is measured. Accordingly, each component of spin-packet motion, i.e. u_1, u_2, u_3 , can be imaged if the experiment is repeated three times and the motion-encoding magnetic-field gradients are aligned to a different axis of an orthogonal reference coordinate system each time.

The amplitude of each spin-packet displacement component, $u_i(x_0, y_0, z_0)$, can be determined directly from the amount of spin phase accrued, $\theta_i(x_0, y_0, z_0, \Phi)$, by a scaling factor proportional to the amplitude, frequency, and duration of the applied motion-encoding gradient, $G_i \sin(\omega_g \tau)$. Sensitivity to motion is greatest when the mechanical actuation frequency, ω_d , and motion-encoding gradient frequency, ω_g , are equal ($\omega = \omega_d = \omega_g$) and the oscillating gradients are synchronized with the applied motion for an integer number of cycles, n . In this case, for sinusoidal encoding and excitation motion, the spin-phase displacement sensitivity can be calculated, in general, as, $\frac{u}{\theta} = \frac{\omega}{\gamma G \pi n}$.

2.2. Steady-state harmonic viscoelastic material response

The mechanical properties of biological tissue may be approximated by fitting measured displacement data to the equations governing wave propagation in an unbounded, isotropic, homogeneous, linear viscoelastic solid. Difficulty in this direct approach arises in selecting the appropriate viscoelastic model *a priori*. The correspondence principle allows the purely elastic equations of motion to be transformed into analogous viscoelastic equations via Laplace or Fourier transform (Lockett 1972, Flügge 1975, Beltzer 1988). As such, invoking the correspondence principle allows the real elastic moduli to be replaced with the *corresponding* complex viscoelastic moduli without requiring a specific rheological model.

The equations of dynamic equilibrium for an unbounded, isotropic, homogeneous, linear elastic solid are

$$\mu u_{i,jj} + (\lambda + \mu)u_{j,ij} = \rho \ddot{u}_i, \quad (i, j = 1, 2, 3) \quad (2)$$

where λ and μ are the elastic (Lamé) parameters of the material; ρ is the material density (typically assumed to be 1000 kg m^{-3} for tissue) and u , and \ddot{u} are the tissue displacement and acceleration, respectively.

In many soft tissues, the dilatational component of motion may be neglected without dramatically affecting estimates of distortional parameters (Manduca *et al* 2001). The velocity of a pressure wavefront in a *nearly* incompressible material (e.g., biological tissue) is approximately 1500 m s^{-1} ; at frequencies up to 2000 Hz (feasible for MRE) the wavelength is greater than 0.75 m, which greatly exceeds the field of view of most MRE experiments. The displacement amplitude of the pressure wave is often sufficiently small that its contribution is within the measurement noise floor. This is especially true if the primary mode of tissue excitation is shear (Sinkus *et al* 2005a), as is the case with our experiments. If the dilatational components of the displacement field in equation (2) are neglected, the following simpler equations are obtained governing *shear wave* propagation in an *elastic* material (Kolsky 1963):

$$\mu u_{i,jj} = \rho \ddot{u}_i \quad (i, j = 1, 2, 3). \quad (3)$$

If the imposed mechanical excitation is harmonic and steady state, the material response at each location in the sample is

$$u_k(x, y, z, t) = (U'_k + iU''_k)e^{i\omega t} + (U'_k - iU''_k)e^{-i\omega t} \quad (k = 1, 2, 3), \quad (4)$$

where $U'_k = U'_k(x, y, z, \omega)$ and $U''_k = U''_k(x, y, z, \omega)$ are the real and imaginary coefficients of the complex exponential. Employing the correspondence principle, the real elastic parameter μ in equation (2) is replaced by the complex shear modulus, $G^*(i\omega)$:

$$\mu \rightarrow G^*(i\omega) = G'(\omega) + iG''(\omega), \quad (5)$$

where G' is the storage modulus and G'' is the loss modulus. In general, both components of the complex modulus depend on frequency. Substituting equations (4) and (5) into equation (3), and separating real and imaginary terms, leads to a coupled set of real equations, recast in terms of the harmonic coefficients:

$$G'U'_{i,jj} - G''U''_{i,jj} = -\rho\omega^2 U'_i \quad (i, j = 1, 2, 3) \quad (6a)$$

$$G'U''_{i,jj} + G''U'_{i,jj} = -\rho\omega^2 U''_i \quad (i, j = 1, 2, 3). \quad (6b)$$

In these equations displacements in orthogonal directions are uncoupled. For this reason, material property estimates can be made from acquisition of any single displacement component. In practice, the displacement component with the largest amplitude, and thus highest contrast-to-noise ratio, is used.

We illustrate the correspondence principle for the specific case of a Voigt material. In terms of Cartesian components, the equations of motion in a Voigt solid take the form (Kolsky 1963)

$$\mu u_{i,jj} + (\lambda + \mu)u_{j,ij} + \eta \dot{u}_{i,jj} + (\varepsilon + \eta)\dot{u}_{j,ij} = \rho \ddot{u}_i \quad (i, j = 1, 2, 3). \quad (7)$$

Here, ε , and η correspond to viscous ‘Lamé constants’, analogous to λ and μ , respectively. Substitution of the expressions for harmonic displacement (4) into equation (7) leads to the relationships

$$\mu U'_{i,jj} + (\lambda + \mu)U'_{j,ij} - \eta \omega U''_{i,jj} - (\varepsilon + \eta)\omega U''_{j,ij} = -\rho \omega^2 U'_i \quad (i, j = 1, 2, 3) \quad (8a)$$

$$\mu U''_{i,jj} + (\lambda + \mu)U''_{j,ij} + \eta \omega U'_{i,jj} + (\varepsilon + \eta)\omega U'_{j,ij} = -\rho \omega^2 U''_i \quad (i, j = 1, 2, 3). \quad (8b)$$

If the dilatational contribution to the displacement field is neglected, the resulting equations (8) are equivalent to equations (6) above with storage modulus $G' = \mu$ and loss modulus $G'' = \eta\omega$.

In some extremely soft, porous tissues in which internal fluid flow occurs readily, the volumetric material distortion may not be negligible. In such cases, algorithms such as numerical Helmholtz decomposition may be employed to remove the contributions of longitudinal waves from experimental displacement fields (Romano *et al* 2005, Sinkus *et al* 2005a, Atay *et al* 2008). Full Helmholtz decomposition is computationally expensive and may introduce additional artifacts (Hackbusch 1985). Alternatively, when data are suspected of containing significant dilatational contributions, the curl of the 3D displacement field can be computed and fitted to the corresponding equations of motion (Sinkus *et al* 2005a, 2005b):

$$\Gamma_i = \varepsilon_{ijk} U_{j,k} \quad (i, j, k = 1, 2, 3), \quad (9)$$

where ε_{ijk} is the Levi–Civita permutation operator. Γ_i is then substituted into equations (6a) and (6b). Note *the divergence of the curl of any vector field is always zero*; thus, $\Gamma_{i,i} = 0$ by definition. Therefore,

$$G' \Gamma'_{i,jj} - G'' \Gamma''_{i,jj} = -\rho \omega^2 \Gamma'_i \quad (i, j = 1, 2, 3) \quad (10a)$$

$$G' \Gamma''_{i,jj} + G'' \Gamma'_{i,jj} = -\rho \omega^2 \Gamma''_i \quad (i, j = 1, 2, 3). \quad (10b)$$

Equations (10a) and (10b) are free of dilatational terms and isolate the transverse components of the full equations of motion.

2.3. Data acquisition

In total, 14 female mice (BALB/cAnNHsd, Harlan), aged 9 to 10 weeks, were studied. Mice were anesthetized with 1.5% isoflurane supplied by nose cone at 1.0 L min⁻¹ oxygen for the duration of all experiments. Body temperature was maintained via a heating pad formed using re-circulating water bath. All procedures were approved by the institutional Animal Studies Committee in accordance with the NIH Guide on the Care and Use of Animals.

Elastography data were obtained in mouse brain at 4.7 T using an Agilent/Varian DirectDriveTM small-animal MR scanner. The scanner consists of an Oxford horizontal-bore magnet, Agilent/Magnex self-shielded gradient coils, and high-performance, gradient power amplifiers (International Electric Company) providing 60 G cm⁻¹ peak magnetic-field gradient amplitude within 0.27 ms. NMR data were collected using an actively decoupled transmit/receive coil pair (Garbow *et al* 2008). A modified spin-echo NMR imaging pulse sequence was used to record spatiotemporal tissue motion as a shift in NMR signal phase (figure 1). There are two noteworthy features of our pulse sequence: (i) sinusoidal motion-encoding magnetic-field gradients are used instead of trapezoidal-shaped gradients, and

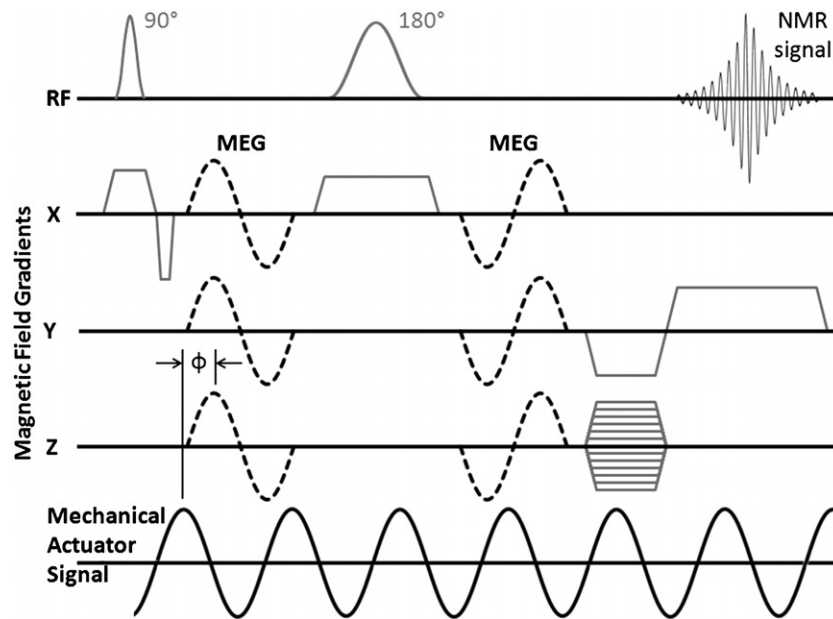


Figure 1. The modified spin-echo magnetic resonance pulse sequence used for elastography data acquisition. In addition to RF and magnetic-field gradient events required to create a spin-echo MRI, sinusoidal, motion-encoding gradients (MEG) are placed on each side of the 180° RF pulse. MEG events and the mechanical actuation signal may be temporally shifted by the parameter ϕ . By varying the delay, ϕ , temporal variations in the wave field are recorded. In this example, a 1-cycle MEG (dashed) is shown on each gradient channel. As a result, motion-encoded phase images are acquired with contrast proportional to displacements perpendicular to an oblique plane in the imaged body.

(ii) harmonic actuator motion is constant throughout the entire experiment to ensure true steady-state tissue response. Instead of toggling the actuator on and off in synchronization with the scanner, the scanner is triggered by the actuator signal.

Propagating shear waves were induced in the brain with the custom-built head holder shown in figure 2. Mechanical vibrations were generated by an amplified-piezoceramic actuator (APA150M-NM, Cedrat Technologies) and transmitted to the mouse via an incisor bar. The actuator was powered by a low-current, high-voltage amplifier (LA75C, Cedrat Technologies). A sinusoidal voltage waveform was supplied to the amplifier by a transistor-transistor logic (TTL) equipped function generator (FG-7002C, Ez Digital Co., Ltd). The MR elastography imaging sequence was set to acquire one line of k -space with each TTL pulse, thereby synchronizing applied mechanical motion with MR motion-encoding gradients. Efficient data acquisition was facilitated by our novel head holder; with only three contact points, animal setup was simple and brief.

The entire mouse brain was imaged with 29 contiguous trans-axial slices in an interleaved manner. Experimental parameters were: resolution, $250 \times 250 \times 250 \mu\text{m}^3$; TR/TE: 1000/27.5 ms; two excitations averaged for each line of k -space. Phase contrast was doubled by acquiring two sets of motion-encoded data, one each with positive and negative polarity motion-encoding gradients, which were subtracted from one another. Actuation frequencies ranged 600–1800 Hz at 200 Hz intervals. The temporal resolution of 600, 800, 1200 and

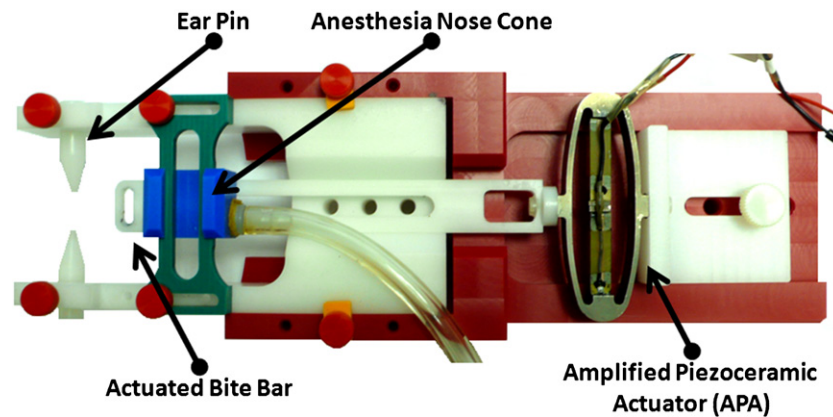


Figure 2. The custom-built stereotaxic mouse head holder used for elastography studies. The head of each mouse was secured between the ear bars and incisor bar. Light tension on the incisor bar ensures contact throughout the actuator stroke. An MR-compatible, amplified piezoceramic actuator drives the incisor bar harmonically, inducing mechanical vibration of the mouse skull along the rostral-caudal axis.

1800 Hz data was 8 points per actuation cycle. The temporal resolution of 1000, 1400 and 1600 Hz data was 4 points per actuation cycle.

Elastography data were acquired for six animals at each mechanical actuation frequency studied. For one animal, at each frequency, all three displacement components, $u_i(x, y, z, t)$, $i = 1, 2, 3$, were acquired at temporal resolution of 4 points per actuation cycle. For all other data, only the through-image-plane component of motion, $u_3(x, y, z, t)$, was recorded. A magnetic-field gradient amplitude of 15 G cm^{-1} was used throughout for motion encoding. TR/TE was held constant for all data; hence, the number of MR motion-encoding gradient cycles varied with the actuation frequency from 3 to 10. Acquiring a complete phase contrast image (i.e. positive and negative polarity images) required approximately 5.5 min per displacement component per time-point for each experiment conducted. Time under anesthesia varied according to test plan and ranged from 23 to 160 min (mean 108 min). All mice survived imaging.

2.4. Data processing

Data post-processing was performed with programs written within the MATLAB (2009b, The MathWorks) computing environment. Motion-sensitized, phase-contrast images were obtained by complex division of positive- and negative-polarity phase images. Parasitic phase wrapping, if present, was removed via commercial software (Phase Vision Ltd). Phase-contrast data were converted into displacements using the phase-displacement sensitivity relation previously discussed, taking into account the factor of two introduced through complex division of positive- and negative-polarity phase images. The fundamental harmonic coefficient, $U'_k + iU''_k$, was extracted by Fourier transform along the time dimension. All data were smoothed with a circular, fourth-order Butterworth bandpass filter (in: 1.52 mm, out: 6.25 mm). A central difference scheme was used to approximate the Laplacian.

Inversion of equations (6a), (6b) and (10a), (10b) was performed via regional least-squares fit. For each voxel, the complex modulus was found that minimized the squared error between the equilibrium equations and data in a kernel surrounding that voxel. The

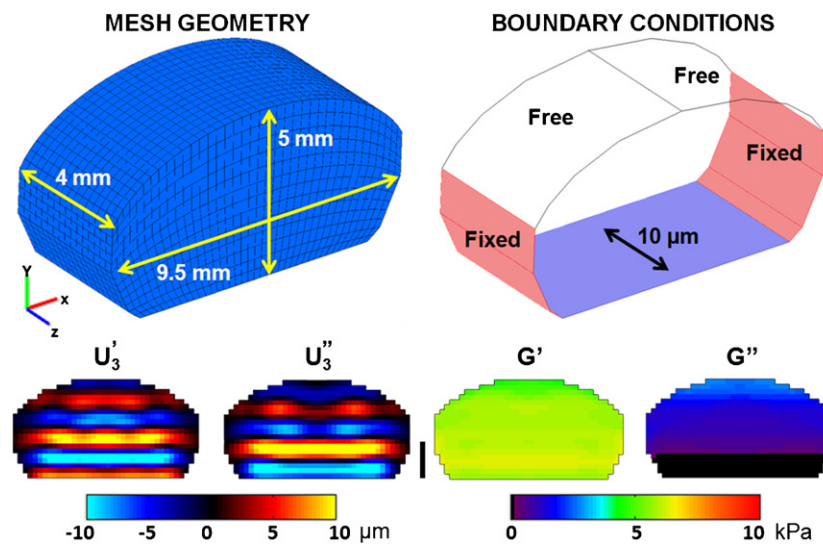


Figure 3. (Top) Finite element model geometry and imposed boundary conditions used for validation of the inversion techniques. (Bottom, left) Real and imaginary parts of the fundamental harmonic displacement component, U_3 . (Bottom, right) Estimates of the viscoelastic parameters shown as functions of the location in the central plane. (2 mm vertical scale bar shown.)

residual error of each fit, normalized by the variance in that kernel, was calculated to assess the ‘goodness-of-fit’ of the linear isotropic homogeneous material model at that location. A normalized residual error (NRE) of zero indicates a perfect local fit; a residual of 1.0, a poor fit.

2.5. Inversion validation

The efficacy of our 1D and 3D inversion schemes were assessed with simulated data generated via finite element analysis (FEA). A numerical model (COMSOL Multiphysics 3.5a, Comsol Inc.) with similar geometry and material dynamics (i.e. attenuation and phase velocity) to those observed experimentally was developed (figure 3). A model discretized by 7904 quadratic hexahedral elements (205 821 degrees-of-freedom) with a nominal side length $250 \mu\text{m}$ was used to simulate the response of a viscoelastic material to harmonic loading. Harmonic frequency analysis was performed at 600, 1200 and 1800 Hz by imposing a harmonic boundary displacement of $10 \mu\text{m}$ to the bottom surface of the brain model. The steady-state response was calculated and data were exported at $250 \times 250 \times 250 \mu\text{m}^3$ resolution, maintaining equivalence between FEA and experimental data.

3. Results

3.1. Inversion validation

Stability and accuracy of our inversion method was assessed using FEA displacement data. A parametric study was conducted to determine the optimal inversion kernel size (N_x, N_y, N_z) and normalized residual error threshold (NRE). For 1D data inversion, the size of the fitting region was defined by $N_x = N_y = 3$; fits with high residual error (NRE > 0.8) were

Table 1. Validation of inversion methods. Estimates of viscoelastic parameters were obtained from simulated (FE) data for each of three inversion methods. (Poisson's ratio of 0.49.)

Frequency (Hz)		Storage modulus, G' (kPa)			Loss modulus, G'' (kPa)		
		Mean	Std	Error	Mean	Std	Error
600	FE Model parameters	2.82	–	–	0.56	–	–
	1D inversion	2.12	0.29	–0.70	0.47	0.16	–0.10
	3D inversion	2.04	0.30	–0.78	0.42	0.12	–0.14
	3D-curl inversion	2.18	0.42	–0.64	0.44	0.16	–0.13
1200	FE model parameters	6.04	–	–	1.21	–	–
	1D inversion	5.88	0.36	–0.16	1.23	0.65	0.02
	3D inversion	5.72	0.43	–0.32	1.09	0.49	–0.12
	3D-curl inversion	5.89	0.83	–0.15	1.16	0.61	–0.04
1800	FE model parameters	14.09	–	–	2.82	–	–
	1D inversion	13.49	0.84	–0.60	2.90	1.46	0.08
	3D inversion	13.15	0.99	–0.95	2.52	1.14	–0.30
	3D-curl inversion	13.55	1.90	–0.54	2.78	1.40	–0.03

rejected. For 3D data inversion, the fitting region was defined by $N_x = N_y = 3$; estimates obtained from poor fits ($NRE > 0.8$) were rejected. Multiple slice planes were incorporated so that through-plane derivatives could be approximated for a single, central plane of data; hence $N_z = 1$ for all analysis. These same parameter values were used for processing of experimental data.

Results from the inversion of simulated data are shown in table 1. The results in this table indicate that over the ranges of material parameters, frequencies and wavelengths observed, errors of less than 1 kPa were typical. At all frequencies, 3D-curl inversion provided storage modulus estimates with greater spatial variation than other methods, as evinced by its higher standard deviation. The storage modulus was consistently under-estimated, regardless of the actuation frequency or analysis scheme. All analysis schemes performed adequately.

3.2. Mouse brain elastography

Experimental data from the largest transaxial plane of mouse brain were processed using the previously discussed methodology. For 1D and 3D inversion, material estimates were made using three contiguous slice planes of data to accommodate numerical calculation of through-plane derivatives required for the Laplacian calculation. Only the through-plane motion component, u_3 , was considered for 1D inversion. All three motion components were considered for 3D inversion. For 3D-curl inversion, five contiguous data slices were selected to accommodate numerical calculation of additional through-plane derivatives required for the curl operation. Data were parsed into three overlapping slice groups, each consisting of three image slices, and the curl was calculated for each group. The central slice from each group was retained such that three contiguous dilatation-free slice planes remained; these data were then run through the existing 3D inversion routine. Representative anatomical images, displacement fields and estimates of material parameters are shown, for each frequency, in figure 4.

Root-mean-square displacement amplitudes of 1.0–2.5 μm are typical in these experiments; amplitudes are smaller at the highest experimental frequencies. The decrease in

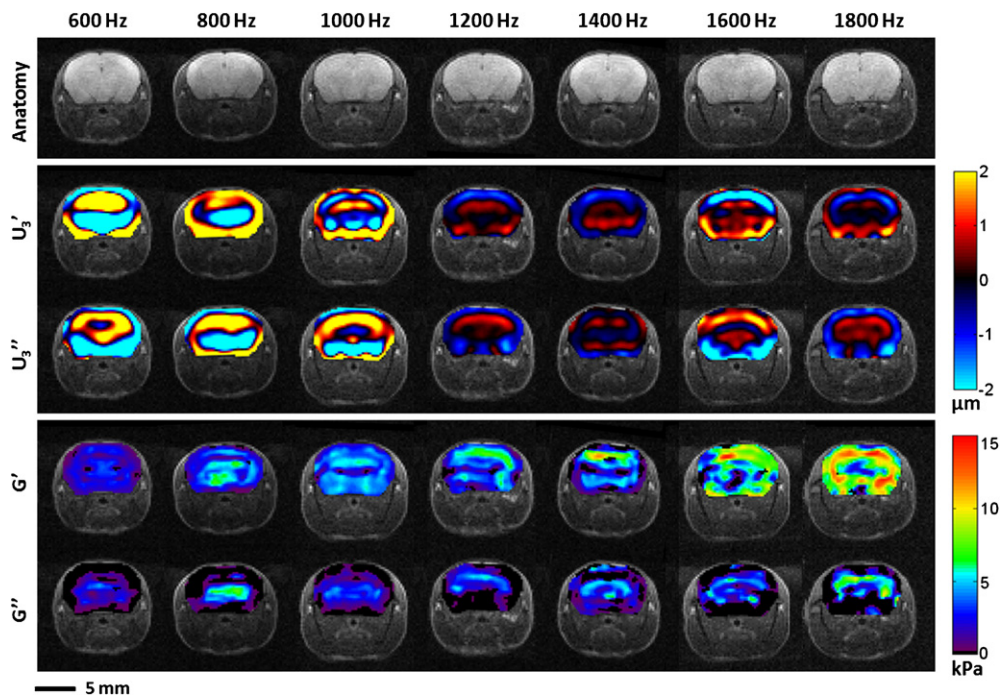


Figure 4. Example anatomical images, displacement fields and estimates of viscoelastic parameters for each excitation frequency. (Row 1) Magnitude images of a central (A/P) region of the brain; four contiguous slices $250 \mu\text{m}$ thick were averaged (1 mm total thickness). (Rows 2 and 3) External mechanical motion induces propagating waves within mouse brain tissue. The real, U_3' , and imaginary, U_3'' , component of the fundamental harmonic of the through-plane displacement is shown for slice two of three contiguous slices used for inversion. (Rows 4 and 5) Elastograms (images of the storage modulus, G' , and loss modulus, G'') calculated from the displacement fields of rows 2 and 3.

amplitude with frequency likely reflects the intrinsic frequency-response characteristics of the actuator itself, as well as reduction in skull transmissibility and increased energy dissipation in brain tissue at these frequencies.

The 1D storage and loss moduli averaged over the entire image plane are reported for each frequency in figure 5. Power-law models of the frequency dependence of storage and loss moduli, fitted independently to each material parameter, are also shown. At each frequency, all three components of the displacement field were acquired for one animal ($n = 1$), thereby permitting use of 3D inversion schemes. Analogous estimates of 3D storage and loss moduli averaged over the entire image plane are presented in figure 6.

4. Discussion

MRE of the mouse brain was performed over a range of frequencies to illuminate the mechanical response of brain tissue. A novel, non-invasive, and versatile actuation system was developed and employed for data collection *in vivo*. The actuator maintained steady harmonic motion and the MR scanner was triggered by the actuation system, which allowed measurement of true steady-state parameter values. The viscoelastic properties of brain were determined

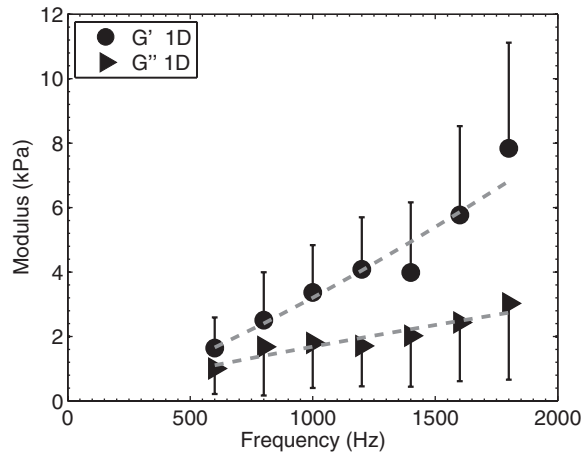


Figure 5. The frequency dependence of the average viscoelastic mechanical parameters estimated for the central region of the mouse brain ($n = 6$). Estimates were obtained by fitting a single motion component of the complex displacement harmonic to equations (6a) and (6b). A power-law fit of the form $G(\omega) = \kappa\omega^\alpha$ is shown as a dashed line. (G' : $\kappa = 0.04 \times 10^{-3}$, $\alpha = 1.29$; G'' : $\kappa = 1.24 \times 10^{-3}$, $\alpha = 0.83$.)

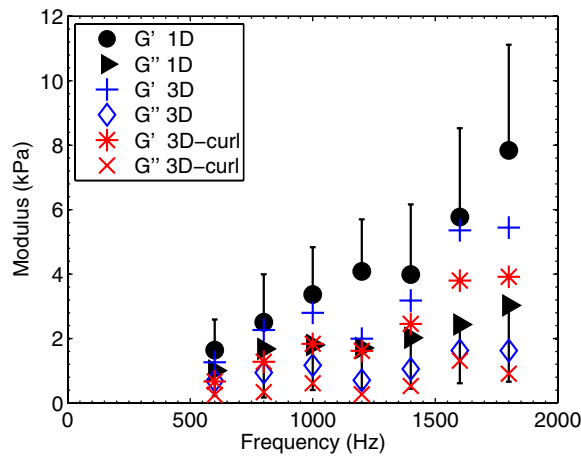


Figure 6. Comparison of the apparent dispersive properties of mouse brain tissue as obtained by three different inversion methods: ‘1D’—equations (6a) and (6b), $i = 3$; ‘3D’—equations (6a) and (6b), $i = 1,2,3$; ‘3D-curl’—equations (10a) and (10b). Mechanical property estimates obtained from fitting 3D displacement fields to the viscoelastic equations of motion are within a standard deviation of estimates obtained by fitting only a single displacement component. (1D: $n = 6$; 3D: $n = 1$.)

over a broad range of driving frequencies, from 600 to 1800 Hz. The averaged material properties of central (A/P) mouse brain matter exhibit pronounced dispersive properties. Both storage and loss moduli of brain tissue depend strongly on the frequency of excitation, which has important ramifications for numerical modeling of TBI.

Previous studies conducted in mouse brain have probed tissue properties at a single driving frequency, within the range of 1000–1500 Hz (Diguet *et al* 2009, Murphy *et al* 2010,

Table 2. Material property estimates of *in vivo* mouse brain tissue measured by MRE.

	Frequency (Hz)	Storage modulus, G'		Loss modulus, G''		Study details		
		Mean	Std	Mean	Std	Strain	Age (wks)	Brain region
		(kPa)	(kPa)	(kPa)	(kPa)			
Atay <i>et al</i> (2008)	1200	13.8	1.49	–	–	C57BL/6	12–15	Central cortical gray matter
Diguet <i>et al</i> (2009)	1000	7.36	0.50	3.33	0.80	C57BL/6	9–11	Central corpus callosum
Schregel <i>et al</i> (2010)	1000	≈5.40	–	≈1.50	–	C57BL/6	–	Corpus callosum
Murphy <i>et al</i> (2010)	1500	26.0	–	–	–	WT	70 ± 2	Central cerebrum
		22.0	–	–	–	APP-PS1	82 ± 2	Central cerebrum

Atay *et al* 2008, Schregel *et al* 2010), cf table 2. In the work by Atay *et al* (2008) and Murphy *et al* (2010), tissue was assumed to be purely elastic and only the apparent elastic shear modulus was estimated. In comparison, viscoelastic material properties obtained in this study, together with those from other studies, reveal variation within an order of magnitude. Differences in the material model assumed for inversion (elastic versus viscoelastic) are clearly responsible for some discrepancies. Other discrepancies may reflect true differences in material properties due to age or analysis region. We do not advocate a specific material model to describe brain tissue viscoelasticity (i.e. a Voigt, Maxwell, springpot, or other analog); rather our results are presented simply as frequency-dependent complex moduli.

Causality of the estimated complex shear modulus was qualitatively assessed by the local Kramers–Kronig (K–K) approximation (Pritz 1999, Madsen *et al* 2008). The exact K–K relations are integral equations that relate the storage and loss moduli over an infinite range of frequencies. Local approximations to the K–K relations (Pritz 1999, Madsen *et al* 2008, O’Donnell *et al* 1981) have been used to demonstrate that a material obeys the principle of causality. The method described by Madsen *et al* (2008) was used to characterize the dispersion relationships observed in this study. Estimates of loss modulus were fit to a polynomial function of $\log(\omega)$, which was then integrated to predict the dispersion of storage modulus. The increases in G' and G'' are consistent with the K–K requirements, but they are not particularly well modeled by the local (approximate) K–K relationship. Nor are both moduli well described by a springpot (single complex power-law) model, as in the studies by Sack *et al* (2009a) and Wuerfel *et al* (2010). However, this is not surprising. The theoretical investigation by Pritz (1999) explains the conditions under which the local K–K approximation is accurate. According to Pritz (1999), if the moduli increase rapidly with frequency (as those of mouse brain tissue appear to) then qualitative, but not quantitative, agreement with the local K–K relations is expected.

MR elastography has limitations. Material property estimates are subject to the constraints of imaging resolution, shear-wave wavelength, and the size of the anatomic feature of interest. It is desirable to have multiple waves in the anatomic region of interest to ensure the accuracy of numerical derivatives. The smaller the anatomic region of interest, the shorter the shear-wave

wavelength required to maintain inversion accuracy. If the material properties are constant, increasing the excitation frequency would lead to a shorter wavelength. However, because of the dispersive properties of biologic tissue (the stiffening of material as actuation frequency increases) an increase in excitation frequency does not proportionally decrease wavelength.

MR imaging resolution determines the spatial-frequency fidelity of elastography data. The Nyquist criterion dictates the shortest wavelength (highest spatial-frequency) detectable in acquired wave-field images. The theoretical minimum wavelength is twice the voxel dimension. In other words, the maximum spatial frequency that can be resolved is half the spatial sampling frequency. In practice, approaching the Nyquist frequency can cause difficulty—oversampling of at least ten times the Nyquist frequency is common in other engineering applications. Unfortunately, as the MR image resolution is increased (voxel size is decreased) the NMR signal amplitude is decreased. Imaging resolution was parametrically evaluated at the start of this study; we concluded that (250 μm) cubic voxels represented the best compromise between imaging resolution, signal-to-noise ratio, and acquisition time at 4.7 T. This is, in fact, the smallest isotropic voxel size used to date in MRE of the mouse brain. Even at this resolution, the finite voxel size does introduce discretization error in the numerical calculations of the Laplacian of the displacement field, which remains a potential source of variation in our estimates of shear modulus.

The majority of the parameter estimates in this study were obtained with a basic 1D inversion technique (analysis of a single component of displacement, obtained throughout the 3D image volume). Because only a single component is acquired, the analysis cannot include a direct Helmholtz decomposition to eliminate displacements due to longitudinal waves. However, estimates from the 1D inversion are very close to estimates obtained in a subset of the animals by a 3D inversion technique in which the curl of the displacement field is used to remove the contributions of longitudinal waves. Both of these estimates are also close to the estimates obtained by a 3D algorithm without the curl operation. While the 3D method using the curl is theoretically the most accurate, it is likely that the estimation of numerical derivatives introduces another source of error (Sinkus *et al* 2005b; cf analysis of FE data in table 1). These results suggest that careful spatial filtering of the raw data to remove the low spatial-frequency (long wavelength) response, combined with the use of our novel actuator setup, which primarily induces shear waves in the brain, effectively mitigate the effects of longitudinal waves. The ability to use a 1D method is important, it reduces the acquisition time by a factor of three and obviates the need to estimate third-order derivatives (required for the curl-based algorithm) or perform computationally intensive Helmholtz decomposition routines (Sinkus *et al* 2005a).

In reality, brain tissue is not only viscoelastic—it is nonlinear, heterogeneous and anisotropic. In this study, displacement-gradients, i.e. strains, were observed to be small, $\frac{\partial u_3}{\partial z} < \frac{\partial u_3}{\partial x} < \frac{\partial u_3}{\partial y} \ll 1$, so kinematic nonlinearity was negligible (figure 7). In contrast, the frequency-dependent trend of calculated mechanical properties presented in figures 5 and 6 indicates the importance of viscoelasticity. Mathematically, without reference to the physics of a particular rheological model, the dispersive properties of mouse brain tissue over the frequencies investigated here are well characterized by a power-law relation of the form $G(\omega) = \kappa\omega^\alpha$. Strain rates increased slightly with increasing actuation frequency (figure 7), which may contribute to the apparent frequency dependence of G'' . It is important to note that mechanical properties reported here are the average values over the entire brain cross-section. The material properties of the brain are not homogeneous, but variations in properties at these length scales are not likely to be captured accurately. As such, anisotropy, which might be expected in the relatively small regions of white matter in the mouse brain, was not

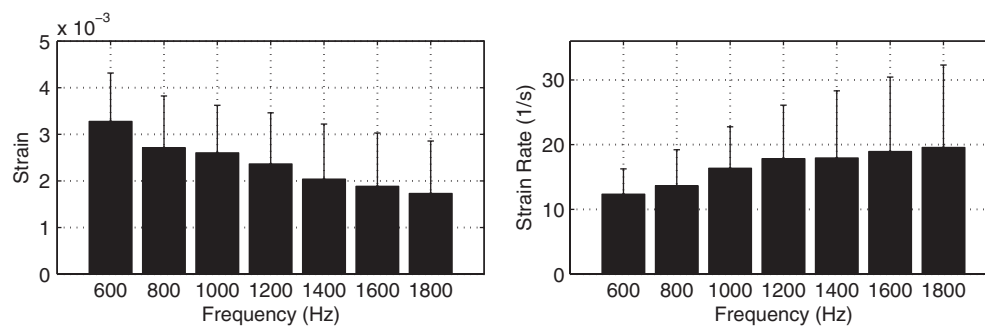


Figure 7. Average, root-mean-square (RMS) shear-strain $\left(\frac{\partial u_3}{\partial y}\right)$ amplitudes (left); and average, RMS shear-strain rates $\left(\frac{\partial^2 u_3}{\partial t \partial y}\right)$ observed in 1D experimental data (right); $n = 6$, standard deviations shown.

investigated. Direct mechanical tests on excised tissue (Prange and Margulies 2002) indicate that directional dependence is weak, even in white matter. Heterogeneity and anisotropy are logical targets for future studies.

5. Conclusions

The average dispersive properties of mouse brain tissue in a central region were estimated *in vivo* using MR elastography. Storage and loss moduli were estimated (i) in all animals by fitting the data to a single component of the equation of motion (1D analysis) and (ii) in a subset of animals by simultaneously fitting all three components of displacement data to the full 3D equation of motion. Results in all cases were similar, and reflected a strong dependence of complex shear modulus (both storage and loss components) on excitation frequency. MRE studies in small animals require motion at high frequencies to propagate shear waves with wavelengths short enough to resolve small features. However, tissue viscoelasticity limits both wavelength and wave penetration depth. Despite these limitations, MRE may provide valuable insight into studies of disease in murine models, and allow pre-clinical evaluations of therapies. Measurements of the viscoelastic parameters of brain tissue at high frequencies are also valuable for modeling and simulation of traumatic brain injury, since TBI results from short-duration events, e.g., blast and impact. The comparison of results from both simulation and experiment provides valuable insight into the quantitative accuracy of MRE.

Acknowledgments

Financial support was provided by NIH RO1 NS055951 (Bayly). Dr Mark Conradi supported MR Tx/Rx coil development. Special thanks to colleagues in the Biomedical Magnetic Resonance Laboratory at Washington University for additional assistance. Numerical simulations performed in this study were made possible by the Cloud computing cluster at Washington University's School of Engineering.

References

- Asbach P, Klatt D, Hamhaber U, Braun J, Somasundaram R, Hamm B and Sack I 2008 Assessment of liver viscoelasticity using multifrequency MR elastography *Magn. Reson. Med.* **60** 373–9

- Atay S M, Kroenke C D, Sabet A and Bayly P V 2008 Measurement of the dynamic shear modulus of mouse brain tissue *in vivo* by magnetic resonance elastography *J. Biomech. Eng.* **130** 021013
- Beltzer A I 1988 *Acoustics of Solids* (Berlin: Springer)
- Chopra R, Arani A, Huang Y, Musquera M, Wachsmuth J, Bronskill M and Plewes D 2009 *In vivo* MR elastography of the prostate gland using a transurethral actuator *Magn. Reson. Med.* **62** 665–71
- Clayton E H, Wang Q, Song S-K and Bayly P V 2010 Non-invasive measurement of vitreous humor stiffness in the mouse using MR elastography *Proc. Int. Society for Magnetic Resonance in Medicine* p 3400
- Diguet E, Van Houten E, Green M and Sinkus R 2009 High resolution MR-elastography mouse brain study: towards a mechanical atlas *Proc. Int. Society for Magnetic Resonance in Medicine* p 714
- Elgeti T, Rump J, Hamhaber U, Papazoglou S, Hamm B, Braun J and Sack I 2008 Cardiac magnetic resonance elastography—initial results *Invest. Radiol.* **43** 762–72
- Flügge W 1975 *Viscoelasticity* (Berlin: Springer)
- Garbow J R, McIntosh C and Conradi M S 2008 Actively decoupled transmit-receive coil-pair for mouse brain MRI *Concepts Magn. Reson. B* **33** 252–9
- Hackbusch W 1985 *Multi-Grid Methods and Applications* (Berlin: Springer)
- Hamhaber U, Sack I, Papazoglou S, Rump J, Klatt D and Braun J 2007 Three-dimensional analysis of shear wave propagation observed by *in vivo* magnetic resonance elastography of the brain *Acta Biomaterialia* **3** 127–37
- Kemper J, Sinkus R, Lorenzen J, Nolte-Ernsting C, Stork A and Adam G 2004 MR elastography of the prostate: initial *in-vivo* application *Rofo. Fortschr. Geb. Rontgenstr. bildgeb. Verfahr.* **176** 1094–9
- Kolipaka A, Araoz P A, Mcgee K P, Manduca A and Ehman R L 2010 Magnetic resonance elastography as a method for the assessment of effective myocardial stiffness throughout the cardiac cycle *Magn. Reson. Med.* **64** 862–70
- Kolsky H 1963 *Stress Waves in Solids* (New York: Dover)
- Kruse S A, Rose G H, Glaser K J, Manduca A, Felmlee J P, Jack C R Jr and Ehman R L 2008 Magnetic resonance elastography of the brain *Neuroimage* **39** 231–7
- Litwiller D V, Lee S J, Kolipaka A, Mariappan Y K, Glaser K J, Pulido J S and Ehman R L 2010 MR elastography of the *ex vivo* bovine globe *J. Magn. Reson. Imaging* **32** 44–51
- Lockett F J 1972 *Nonlinear Viscoelastic Solids* (London: Academic)
- Madsen E L, Frank G R, Hobson M A, Lin-Gibson S, Hall T J, Jiang J and Stiles T A 2008 Instrument for determining the complex shear modulus of soft-tissue-like materials from 10 to 300 Hz *Phys. Med. Biol.* **53** 5313–42
- Manduca A, Oliphant T E, Dresner M A, Mahowald J L, Kruse S A, Amromin E, Felmlee J P, Greenleaf J F and Ehman R L 2001 Magnetic resonance elastography: non-invasive mapping of tissue elasticity *Med. Image Anal.* **5** 237–54
- Murphy M C, Curran G L, Glaser K J, Rossman P J, Huston J, Poduslo J F, Jack C R, Felmlee J P and Ehman R L 2010 MR Elastography of the brain in a mouse model of Alzheimer's disease *Proc. Int. Society for Magnetic Resonance in Medicine* p 2360
- Muthupillai R, Lomas D J, Rossman P J, Greenleaf J F, Manduca A and Ehman R L 1995 Magnetic resonance elastography by direct visualization of propagating acoustic strain waves *Science* **269** 1854–7
- Muthupillai R, Rossman P J, Lomas D J, Greenleaf J F, Riederer S J and Ehman R L 1996 Magnetic resonance imaging of transverse acoustic strain waves *Magn. Reson. Med.* **36** 266–74
- O'Donnell M, Jaynes E T and Miller J G 1981 Kramers–Kronig relationship between ultrasonic attenuation and wave velocity *J. Acoust. Soc. Am.* **69** 696–701
- Pattison A J, Lollis S S, Perrañez P R, Perreard I M, McGarry M D J, Weaver J B and Paulsen K D 2010 Time-harmonic magnetic resonance elastography of the normal feline brain *J. Biomech.* **43** 2747–52
- Plewes D B, Bishop J, Samani A and Sciarretta J 2000 Visualization and quantification of breast cancer biomechanical properties with magnetic resonance elastography *Phys. Med. Biol.* **45** 1591–610
- Prange M T and Margulies S S 2002 Regional, directional, and age-dependent properties of the brain undergoing large deformation *J. Biomech. Eng.* **124** 244
- Pritz T 1999 Verification of local Kramers–Kronig relations for complex modulus by means of fractional derivative model *J. Sound Vib.* **228** 1145–65
- Robert B, Sinkus R, Gennison J-L and Fink M 2009 Application of DENSE-MR-elastography to the human heart *Magn. Reson. Med.* **62** 1155–63
- Romano A J, Abraham P B, Rossman P J, Bucaro J A and Ehman R L 2005 Determination and analysis of guided wave propagation using magnetic resonance elastography *Magn. Reson. Med.* **54** 893–900
- Rouviere O, Yin M, Dresner M A, Rossman P J, Burgart L J, Fidler J L and Ehman R L 2006 MR elastography of the liver: preliminary results *Radiology* **240** 440–8
- Sack I, Beierbach B, Wuerfel J, Klatt D, Hamhaber U, Papazoglou S, Martus P and Braun J 2009a The impact of aging and gender on brain viscoelasticity *Neuroimage* **46** 652–7

- Sack I, Rump J, Elgeti T, Samani A and Braun J 2009b MR elastography of the human heart: noninvasive assessment of myocardial elasticity changes by shear wave amplitude variations *Magn. Reson. Med.* **61** 668–77
- Schregel K, Wuerfel E, Wuerfel J, Petersen D and Sinkus R 2010 Viscoelastic properties change at an early stage of cuprizone induced affection of oligodendrocytes in the Corpus Callosum of C57/black6 mice *Proc. Int. Society for Magnetic Resonance in Medicine* p 2134
- Sinkus R, Tanter M, Catheline S, Lorenzen J, Kuhl C, Sondermann E and Fink M 2005a Imaging anisotropic and viscous properties of breast tissue by magnetic resonance-elastography *Magn. Reson. Med.* **53** 372–87
- Sinkus R, Tanter M, Xydeas T, Catheline S, Bercoff J and Fink M 2005b Viscoelastic shear properties of *in vivo* breast lesions measured by MR elastography *Magn. Reson. Imaging* **23** 159–65
- Wuerfel J, Paul F, Beierbach B, Hamhaber U, Klatt D, Papazoglou S, Zipp F, Martus P, Braun J and Sack I 2010 MR-elastography reveals degradation of tissue integrity in multiple sclerosis *Neuroimage* **49** 2520–5
- Yin M, Talwalkar J, Glaser K, Manduca A, Grimm R, Rossman P, Fidler J and Ehman R 2007a Assessment of hepatic fibrosis with magnetic resonance elastography *Clin. Gastroenterol. Hepatol.* **5** 1207–13.e2
- Yin M, Woollard J, Wang X, Torres V E, Harris P C, Ward C J, Glaser K J, Manduca A and Ehman R L 2007b Quantitative assessment of hepatic fibrosis in an animal model with magnetic resonance elastography *Magn. Reson. Med.* **58** 346–53